Effect of over-aging on the microstructural evolution in an Al–Cu–Mg–Ag alloy during ECAP at 300 °C

Marat Gazizov , Rustam Kaibyshev

Keywords:
High-temperature alloy
Metals and alloys
Microstructure
Precipitation
Phase transitions
Scanning electron microscopy

ABSTRACT

This report explores over-aging as it relates to microstructural evolution during equal channel angular pressing (ECAP) at 300 °C using a novel Al–Cu–Mg–Ag alloy doped with zirconium and scandium. Material characterization was conducted using scanning electron microscopy (SEM), transmission electron microscopy (TEM) and X-ray analysis in which microstructural evolution in a quenched alloy (QA) material was compared to that in an over-aged alloy (OA) material. It was shown that over-aging facilitates grain refinement where, at $\varepsilon \sim 12$, a fraction of the high angle boundaries (HABs) and average misorientation angles are ~0.72 and 30°, respectively. In contrast, a partially recrystallized structure evolves in the QA sample even after $\varepsilon \sim 12$. Intense plastic straining affects precipitation. In the QA, ECAP leads to the precipitation in Ω-phase with a plate-like shape, initially. Further strain leads to a shearing offset associated with a localized dislocation glide followed by dissolution of Ω-phase and precipitation of the θ-phase (Al_2Cu) and S-phase (Al_2CuMg), both of which share an equaxed shape. In the OA, the dissolution of the Sc enriched θ-phase consisting of relatively coarse particles is followed by precipitation of nanometer-sized scale dispersoids of a Sc depleted θ-phase on deformation-induced boundaries. In addition, Ag and Mg-rich particles being β′(MgAg) and U(AlMgAg) phases precipitate during ECAP, in both states of the Al–Cu–Mg–Ag alloy explored herein.

1. Introduction

Currently, there is considerable interest in the fabrication of ultrafine-grained (UFG) aluminum alloys by severe plastic deformation (SPD) through equal channel angular pressing (ECAP) [1]. The formation of the UFG structure can improve strength significantly in accordance with the Hall–Petch relationship and provide exceptionally high superplastic properties [1,2], even in age-hardened aluminum alloys containing Sc where the UFG structure is retained under solution treatment [2–5]. The UFG structure in Al–Cu alloys can be produced by ECAP [1,6–8]. However, aluminum alloys are materials with a high value of stacking fault energy. Consequently, extensive dynamic recovery highly decreases density of lattice dislocations [9], and Al–Cu alloys exhibit a low rate of dynamic recrystallization (DRX), especially when $T \geq 300$ °C [7]. As a result, in these alloys the UFG structure can be produced by imposing very high plastic strains. The formation of fully recrystallized structure at a higher temperature could be accelerated due to particle stimulated nucleation (PSN) [10,11]. For instance, a fully recrystallized structure is evolved at $\varepsilon \sim 8$ and $T = 250$ °C in the AA2219 alloy [6].

Introducing nanoscale dispersoids [7,8] or primary particles with an average size of 2 μm [10] facilitates grain refinement; aluminum alloys containing dispersoids or particles exhibit a high rate of DRX during ECAP compared to a dilute aluminum alloy [8,10]. However, it is well known that coarse particles deteriorate the crack resistance of aviation grade aluminum alloys. Therefore, it is best to use particles with thermodynamically equilibrium phases as this may decrease the amount of straining necessary for aluminum alloys to produce a UFG structure. This phase precipitates during over-aging and dissolves during subsequent solution treatment and, therefore, could not affect final mechanical properties. However, the average particle size precipitated during the over-aging process is significantly less than 1 μm. The positive effect of these particles on grain refinement during ECAP is not obvious [10,11].

The goal of this study is to consider the effect of over-aging on grain refinement during ECAP in an Al–Cu–Mg–Ag alloy. It is known that alloys belonging to Al–Cu–Mg–Ag system have a unique phase composition. The Mg and Ag additions provide the formation of the Ω-phase, which is coherent modification of the equilibrium θ-phase (Al_2Cu) [6–9,12–16]. The Ω-phase forms as a uniform dispersion of nanoscale hexagonal platelets with $\{1\,1\,1\}_\alpha$ habit planes in peak aged Al–Cu–Mg–Ag alloys. Atomic layers of the segregation of Ag and Mg to the coherent Ω/Al interface occurs because it lowers the interfacial energy of the $(0\,0\,1)\Omega||(1\,1\,1)_\alpha$ interface and aids in accommodation of the misfit that exists between the Ω-phase and the Al lattice [14,15]. The Ω-phase maintains coherency along the $\{1\,1\,1\}_\alpha$ planes at temperatures up to 200–250 °C [14,17,18]. However, the Ω-phase is metastable under conditions of aging at $T \geq 250$ °C [18]. It is known that over-aging leads eventually to the replacement of the Ω-phase by the equilibrium θ-phase. Therefore, we can expect that phase compositions of the Al–Cu–Mg–Ag alloy and the AA2219 alloy [6,7] after over-aging will be essentially the same, and, therefore, over-aging may highly promote grain refinement during ECAP in the both alloys.

2. Experimental details

An aluminum alloy with the chemical composition Al–5.6Cu–0.72Mg–0.5Ag–0.17Sc–0.12Zr–0.32Mn–0.07Ti–0.1Ge–0.02Ni–0.03Fe–0.01Si–0.02 V (mass%) was prepared by a semi-continuous casting method. Next, ingots with dimensions of ⌀40 mm × 120 mm were subjected to a two-step homogenization annealing at 360 °C for 6 h, followed by subsequent heating to 510 °C and soaking for 24 h. Rods with dimensions of 20 mm × 20 mm × 100 mm were machined from the central part of these ingots. These machined rods were solution-treated at 520 °C for 2 h and subsequently water quenched. This state of the alloy will be denoted as the quenched alloy (QA) throughout this paper. Next, parts of solution-treated rods were over-aged at 380 °C for 3 h to produce a two-phase microstructure. The state of this alloy will be denoted as the over-aged alloy (OA) throughout this paper.

Following these preparative steps, the ECAP processing was carried out using an isothermal die with a square internal cross-section of 20 mm × 20 mm. The channel had an L-shaped configuration, with an angle of intersection of 90° and an outer arc curvature angle of ~1°. Deformation through these angles produces a strain of ~1 on each passage through the die [1,19]. The QA and OA samples were extruded to several strains (namely: 1, 2, 4, 8 and 12 passes) at 300 °C. A back pressure of 20% ram pressure was applied to accelerate the grain refinement process and produce the flawless billet. The route B_C, in which the sample is rotated by 90° in the same direction between each pass [1,19] was used. The amount of time for which a specimen was held at deformation temperature during ECAP processing was about 3 min per press.

The discs of mechanically thinned samples were electropolished in a solution of 30% HNO_3 and 70% CH_3OH at −30 °C using a Tenupol-5 twin-jet polishing unit for transmission electron microscopy (TEM). The thin foils were examined using a FEI TECNAI-G^2 TEM with a double-tilt stage and a field emission gun operated at 200 kV. This TEM was equipped with an EDAX energy dispersive X-ray analyzer. The average dislocation density was estimated by counting intersection points of dislocations with the thin foil surface [20]. The volume fraction of the secondary phase particles was calculated by using points counting on the grid method [21]. Metallographic analysis was carried out using an Olympus GX71 optical microscope after etching by standard Keller's reagent. Orientation imaging microscopy (OIM) with automated indexing of electron back scattering diffraction (EBSD) patterns was performed in a FEI Quanta 600FEG scanning electron microscope (SEM) with OIM analysis software provided by TexSem Lab Inc. Notably, black and white lines on the EBSD maps indicate the HABs (≥15°) and low-angle boundaries (LABs) (2–15°), respectively. The average crystallite size was measured by the mean linear intercept method. The terms 'grain' and 'subgrain' are used to define the crystallites, which are entirely delimited by the HABs and LABs, respectively [22]. The '(sub)grains' are crystallites which are bound partly by LABs and partly by HABs [22]. The volume fraction of grains was deemed to be the 'recrystallized' fraction [22].

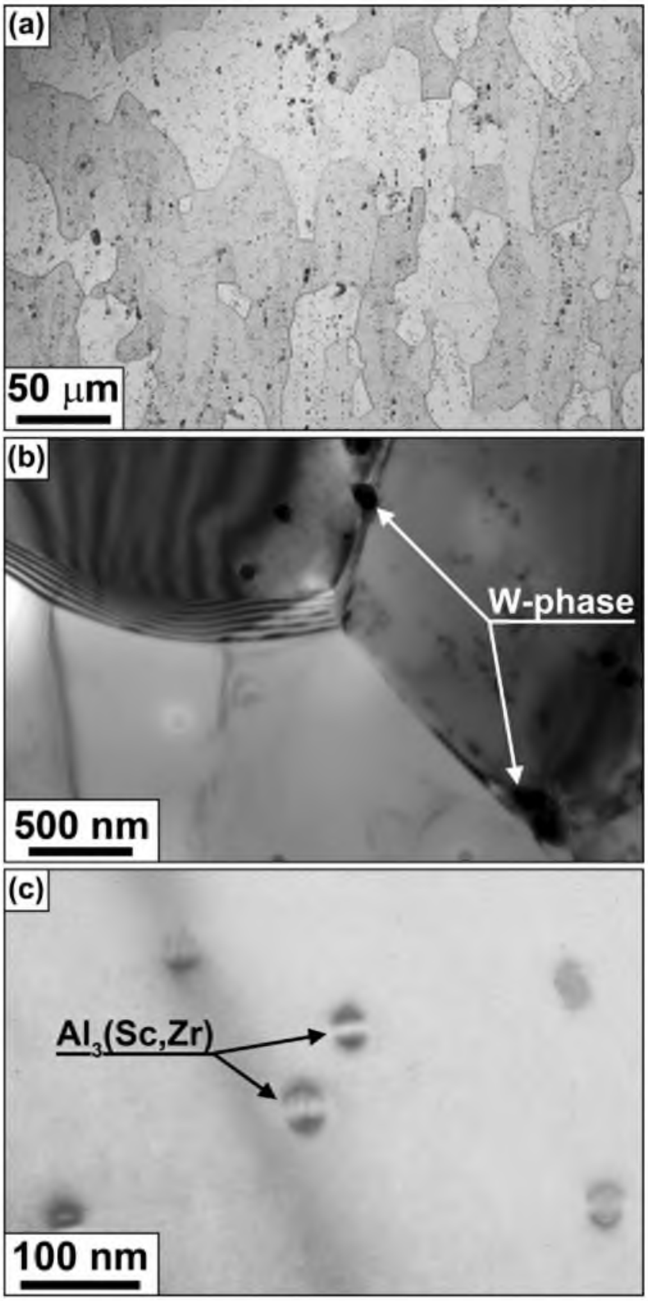

Fig. 1. Representative QA structure observed by optical microscopy (a) and bright-field TEM (BF-TEM) (b,c).

Phase analysis was carried out by X-ray diffraction (XRD) using a Rigaku Ultima IV diffractometer equipped with a Cu K_α radiation source and a semiconductor detector. The samples were scanned from 15 to 70 degrees over 2θ at an angular velocity of 2°/min.

3. Results

3.1. Microstructure before deformation

The initial microstructure of the alloy after solution treatment was previously described in detail [23]. It is worth noting that the structure of the QA is essentially the same where initial grains have average dimensions of ~48 and ~30 μm in the longitudinal and transverse direction, respectively, and particles with the primary θ-phase and ternary W-phase ($Al_{8-x}Cu_{4+x}Sc$) [23] were situated on grain boundaries (Fig. 1). The determined volume fraction and average particle size for these materials are ~2.6% and ~150 nm, respectively, with an inter-particle spacing of ~1 μm. In addition, a dispersion of coherent particles containing the $Al_3(Sc,Zr)$ phase (average particle size ~25 nm) was found within the interiors of most grains (Fig. 1c). Their distribution is non-uniform, and the inter-particle spacing ranges from 100 nm on the short end up to 10 μm on the large end.

Over-aging leads to an increase in the overall volume fraction of the secondary phase particles up to ~17% (Fig. 2). Most of precipitates are the θ-phase exhibiting an equiaxed shape (average particle size ~170 nm) (Figs. 2 and 3). This phase is enriched by Sc and Zr (Fig. 3a) and precipitates within the interiors of initial grains and along the grain boundaries (Fig. 2). The average inter-particle spacing measured by image analysis was ~0.5 μm. In addition, nanoscale Cu enriched Al_6Mn dispersoids having a well-defined plate-like shape with a longitudinal dimension of ~ 250 nm are rarely observed (Figs. 2 and 3c); their volume fraction is negligible. It is obvious that precipitation of this phase under over-aging is not important for grain refinement during ECAP. Thus, the over-aging at a relatively high temperature of 380 °C leads to the precipitation of the Sc-enriched θ-phase [23], mainly. Hence, the main difference in a dispersion of secondary phases between the present alloy and the AA2219 alloy in the over-aged condition [6,7] is in the chemical composition of θ-phase.

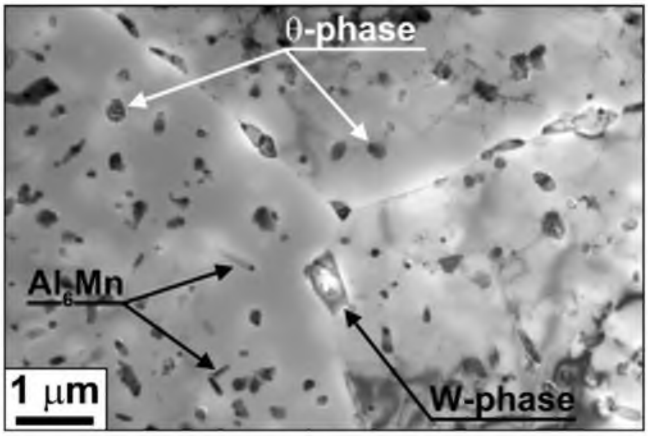

Fig. 2. Representative OA structure observed by BF-TEM.

It is worth noting that W-phase particles having an equiaxed shape (average size of ~500 nm) are observed after over-aging on grain boundaries (Fig. 3b). Particles of this phase contain 5.3% Sc and 1.2% Zr on average. However, careful structural observation did not reveal difference in volume fraction, morphology and chemical composition between particles of W-phase observed in the QA and OA. It is apparent that that these particles of ternary W-phase precipitated under homogenization annealing [23].

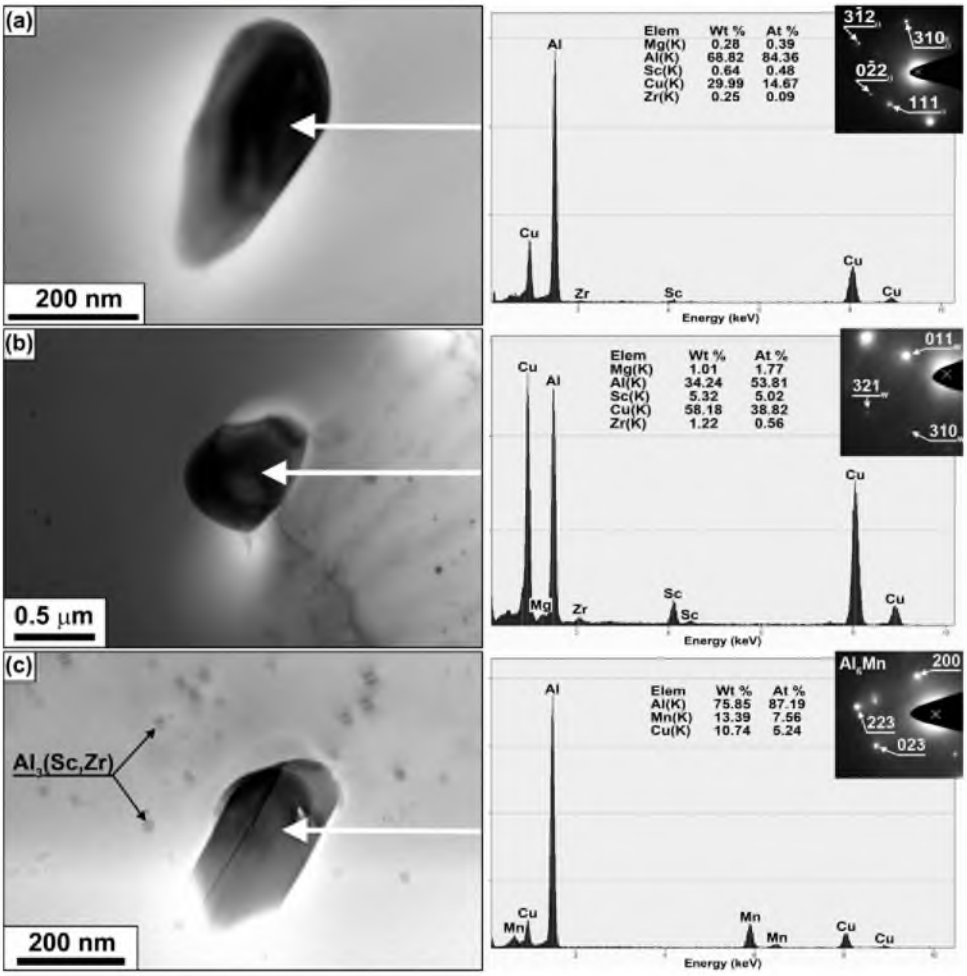

Elem	Wt %	At %
Mg(K)	0.28	0.39
Al(K)	68.82	84.36
Sc(K)	0.64	0.48
Cu(K)	29.99	14.67
Zr(K)	0.25	0.09

Elem	Wt %	At %
Mg(K)	1.01	1.77
Al(K)	34.24	53.81
Sc(K)	5.32	5.02
Cu(K)	58.18	38.82
Zr(K)	1.22	0.56

Elem	Wt %	At %
Al(K)	75.85	87.19
Mn(K)	13.39	7.56
Cu(K)	10.74	6.24

Fig. 3. The phase composition of the OA material is shown, depicting the θ-phase (a), W-phase (b), Al_6Mn and $Al_3(Sc,Zr)$ phases (c).

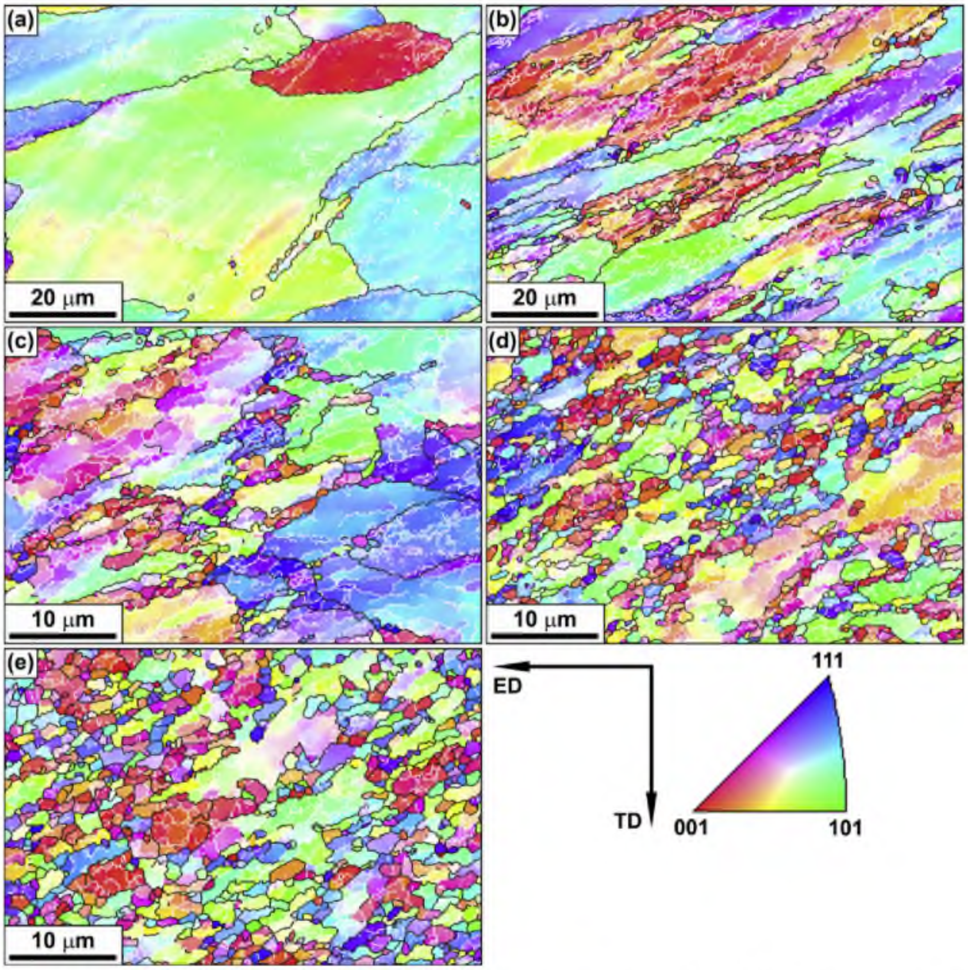

Fig. 4. Microstructural evolution of the QA material subjected to ECAP with strains of $\varepsilon \sim 1$ (a), $\varepsilon \sim 2$ (b), $\varepsilon \sim 4$ (c), $\varepsilon \sim 8$ (d) and $\varepsilon \sim 12$ (e).

3.2. Microstructural evolution associated with ECAP of the quenched alloy

EBSD maps and TEM images of the deformation microstructure of the QA material after multiple passes with ECAP are shown in Figs. 4 and 5, respectively. After $\varepsilon \sim 1$, the initial grains are elongated along the shearing plane [1] (Fig. 4a). These grains are divided by extended planar dislocation boundaries with low-to-moderate misorientation that occur parallel or perpendicular to the shearing plane. These LABs are termed as geometrically necessary boundaries (GNBs) forming between regions of different strain patterns to accommodate the accompanying difference in lattice rotation [24] and comprising deformation bands within some grains. Fig. 4a depicts a microstructure consisting of lamellar subgrains aligned to the direction of the ECAP die's shear plane. The LABs spacing in normal direction (ND) is higher than 2.8 μm. A moderate dislocation density is observed within these elongated subgrains (Table 1).

Table 1
Average dislocation density measured in the alloy subjected to ECAP.

Number of passes	Prior QA (m^{-2})	Prior OA (m^{-2})
1	3.5×10^{13}	1×10^{13}
2	6×10^{13}	4×10^{13}
4	5.5×10^{13}	3×10^{13}
8	2.5×10^{13}	1.5×10^{13}
12	2×10^{13}	1.5×10^{13}

TEM analysis identified a high density of plates having coherent boundaries precipitating along the $\{1\,1\,1\}_{Al}$ planes (Fig. 6a). These particles were identified as being Ω-phase [12–15,23] with longitudinal and transverse dimensions of ~36.2 and ~5.6 nm, respectively. There is good evidence for strong coherency-strain fields caused by a misfit between the lattice of the Ω-phase and the aluminum matrix.

After $\varepsilon \sim 2$, the deformation microstructure consists of lamellar subgrains aligned along the shear plane (Fig. 4b). The average boundary spacing ranges from 1.5 to 2.5 μm. A second ECAP press leads to increased density of the GNBs with low-to-moderate angle misorientation where the density of randomly distributed lattice dislocations is increased by a factor of 2 (Table 1). However, a little subdivision of lamellar subgrains occurs as a result of the formation of incidental dislocation boundaries (IDBs) [24] causing the rearrangement of lattice dislocations and the random trapping of mobile dislocations [22]. The formation of recrystallized grains takes place in the vicinity of triple junctions and on some initial boundaries.

After $\varepsilon \sim 2$, the average dimensions of Ω-phase particles are ~31.9 and ~9.8 nm in longitudinal and transverse directions, respectively (Figs. 6b and 7a). Hence, during ECAP the plate thickness of the Ω-phase increases to ~9.8 nm similarly with the artificial aging process at 300 °C [14,18]. A decrease in the length of the Ω-phase plates occurs by shear offsets (Fig. 8c) due to the passage of several dislocations on the same plane through these particles [12,13]. Localization of dislocation glide takes place in the

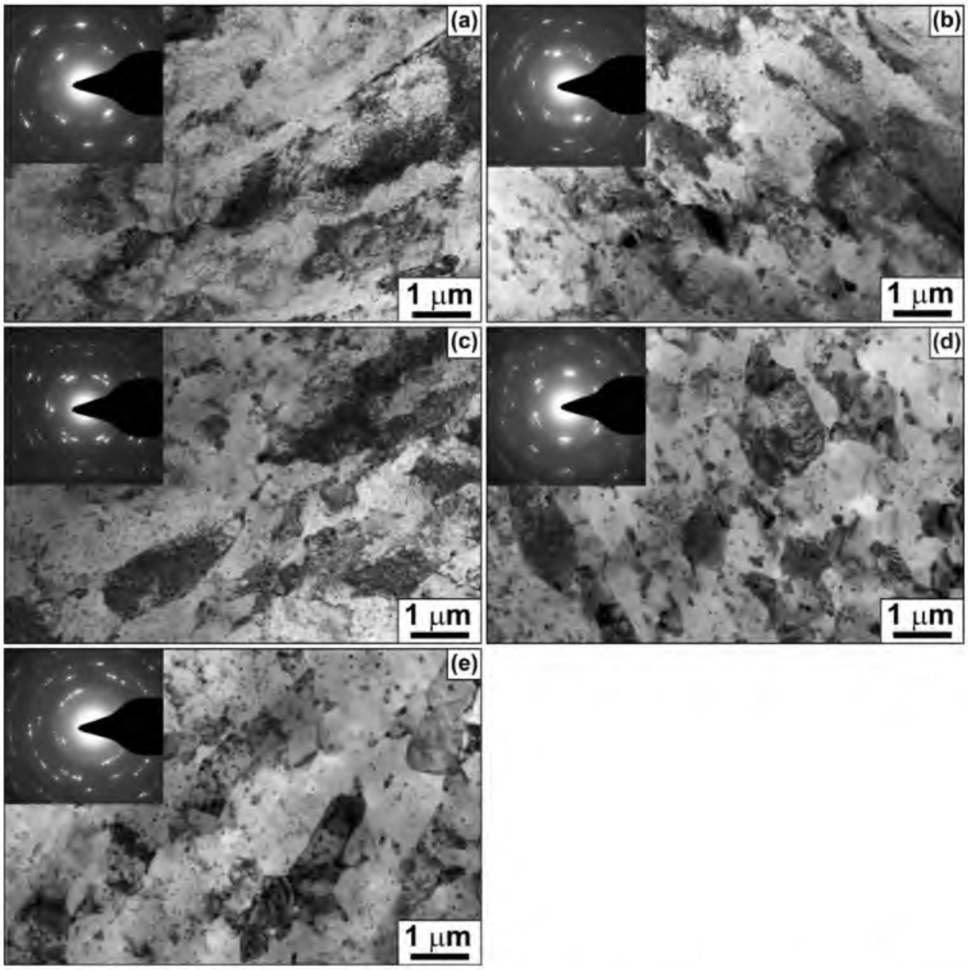

Fig. 5. Representative BF-TEM microstructures with diffraction patterns of the QA after ECAP with strains of $\varepsilon \sim 1$ (a), $\varepsilon \sim 2$ (b), $\varepsilon \sim 4$ (c), $\varepsilon \sim 8$ (c) and $\varepsilon \sim 12$ (e).

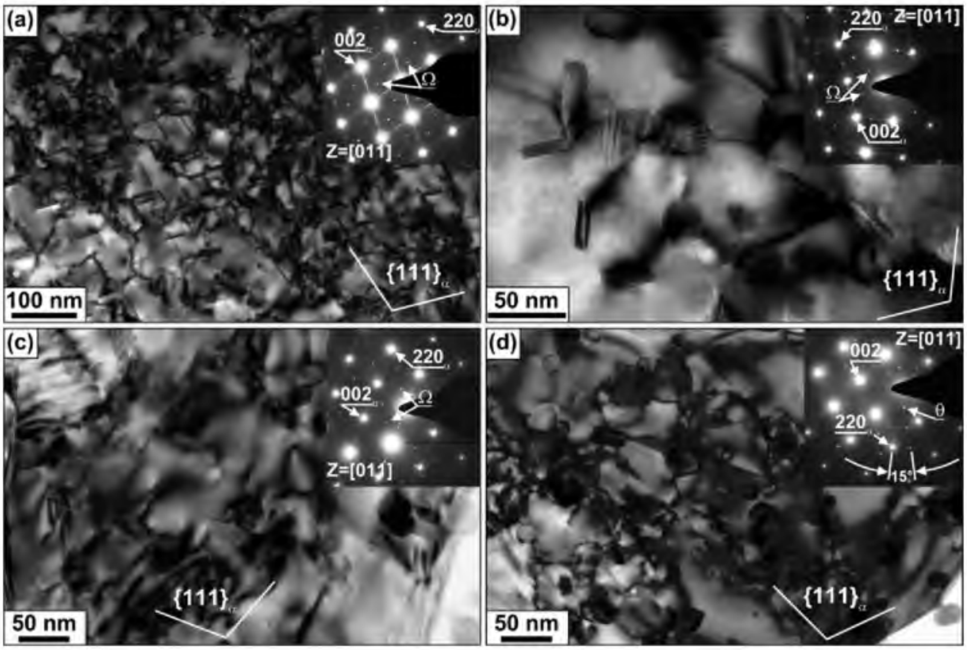

Fig. 6. BF-TEM images of the Ω precipitates in the QA after ECAP with strains of $\varepsilon \sim 1$ (a), $\varepsilon \sim 2$ (b), $\varepsilon \sim 4$ (c) and $\varepsilon \sim 8$ (d).

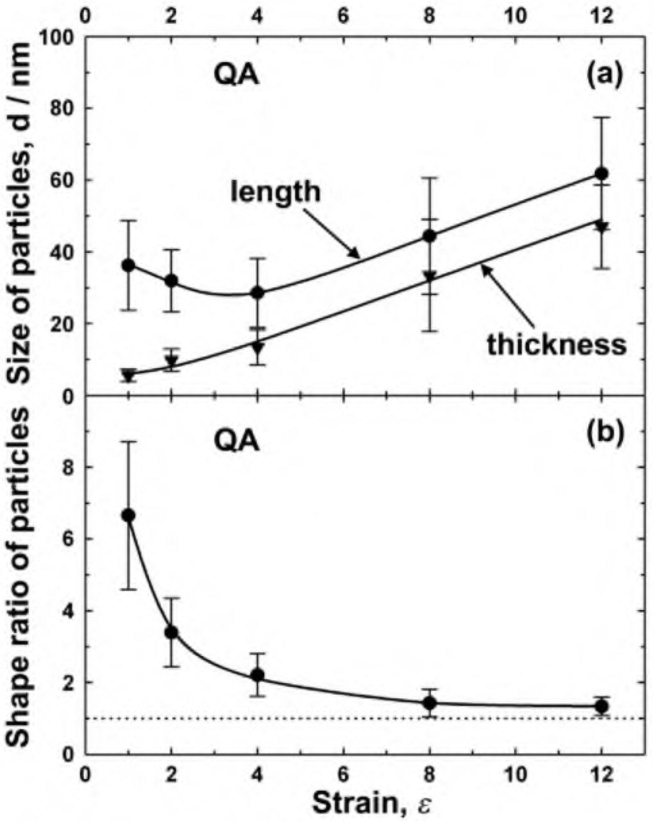

Fig. 7. Effect of strain on size (a) and shape ratio of particles (b) in the QA.

primary slip system at 300 °C that is in contrast with room temperature [12]. This is why the spacing between each cut is >20 nm (Fig. 8c) that is more than four-fold higher in comparison with this spacing observed at room temperature [12].

The heterogeneous nucleation of S-phase (Al_2CuMg) particles on the plate ends of the Ω-phase is observed (Fig. 8a and b). It was found that the orientation of S-phase particles obeys to one of the orientation relationships equivalent to $[1\,0\,0]_\alpha//[1\,0\,0]_S$, $[0\,2\,{-1}]_\alpha//[0\,1\,0]_S$ and $[0\,1\,2]_\alpha//[0\,0\,1]_S$ [25].

After $\varepsilon \sim 4$, the deformation structure constitutes deformation bands separated by HABs or GNBs with low-to-moderate angle misorientation. Average thickness of these deformation bands is ~1 μm (Figs. 4c and 5c). These bands are usually situated near initial boundaries. In addition, numerous grains and (sub)grains are observed in triple junctions and on initial boundaries. The formation of LABs takes place within these crystallites (Fig. 4c).

After eight passes, individual band structures were no longer distinguishable, and a mantle of recrystallized grains [11] evolved on initial boundaries (Fig. 4d). (Sub)grains and grains exhibit equiaxed shape (Fig. 5d). GNBs with low-to-moderate angle misorientation could be distinguished within areas that have not been recrystallized yet (Fig. 4d). A decrease in the average dislocation density is observed (Table 1). A transformation of particles from the Ω-phase to the θ-phase occurs by a gradual loss of their orientation relationship with the matrix (Fig. 6d). It is seen, Ω-phase particles having plate-like shape and coherent or semi-coherent interfaces are substituted by θ-phase particles having an equiaxed shape with an average size of ~ 40 nm (Fig. 7) with strain. These particles have incoherent boundaries and most of them are situated on grain boundaries. In general, particles of different origin after intense plastic straining acquire an equiaxed shape (Fig. 9). However, some coarse particles with the S-phase exhibit a rod-like shape (Fig. 9).

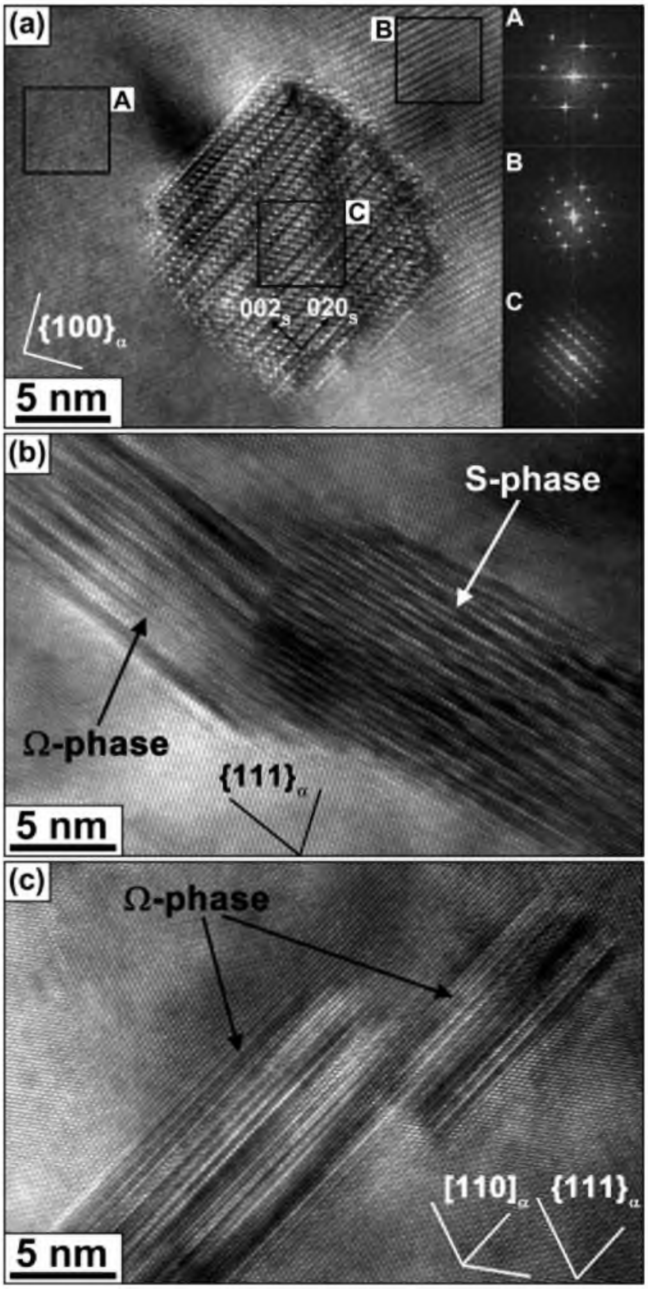

Fig. 8. Particles of Ω and S-phases after two passes of ECAP using QA materials and moduli of their Fourier transforms: matrix (A), Ω-phase (B) and S-phase (D). Zone axis of $[0\,0\,1]$ (a) and $[0\,1\,1]$ (b, c).

Processing to $\varepsilon \sim 12$ leads to the formation of a partially recrystallized structure (Fig. 4e) where small areas that have not been recrystallized could be found within the core region of the initial grains. At the same time, recrystallized grains are dominant within mantle region [11] while (sub)grains are rarely observed. Hence, no formation of the fully recrystallized structure occurs in the QA material due to low rate of DRX within the core region. The primary mechanism of extensive grain refinement, continuous DRX (CDRX), occurs in a highly heterogeneous manner throughout the formation of deformation bands followed by their transformation to the mantle of recrystallized grains. This recrystallization process remains incomplete even after $\varepsilon \sim 12$. A significant agglomeration of particles containing a mixture of the θ- and S-phases with an average size of ~60 nm is observed (Fig. 7). No evidence for the presence of Ω-phase platelets was found after $\varepsilon \sim 12$.

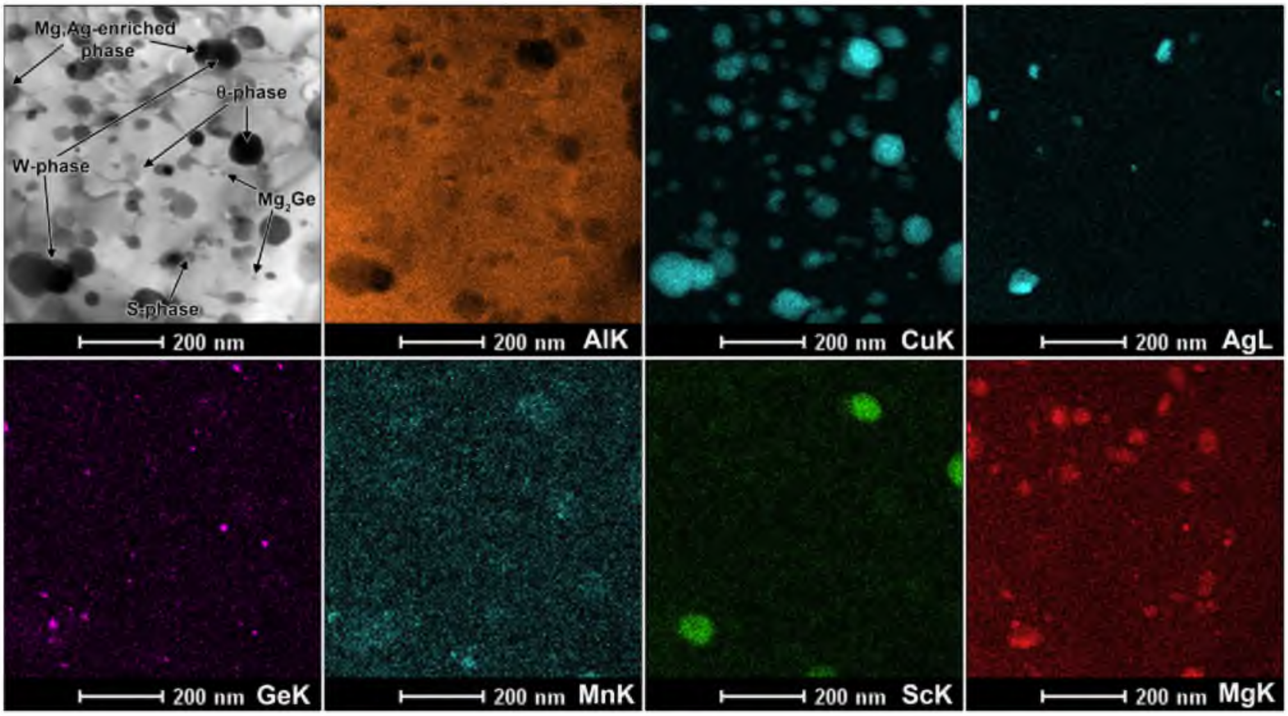

Fig. 9. Scanning TEM (STEM) image and distribution of Al, Cu, Ag, Ge, Mn, Sc and Mg in selected plane after 8 passes ECAP using the QA material.

Generally speaking, it is possible to conclude that intense plastic deformation leads to the precipitation of coherent plates with the Ω-phase, and these particles lose their coherency as a dispersion of θ- and S-phase particles having equiaxed shape and incoherent boundaries evolves (Figs. 7 and 9). At 300 °C, the last phases are more thermodynamically equilibrium than the Ω-phase and these phases grow at the expense of the less-stable Ω-phase in accordance with well-known Gibbs–Thomson schema [26]. In addition, relatively coarse particles of two other phases containing Sc and Mg with Ag could be detected (Fig. 9), and fine particles containing Ge are distinguished. The coarse particles, which were not found after homogenization annealing [23], precipitate during ECAP, and the fine particles form as the primary phase in the melt on solidification [23].

X-ray diffraction experiments (Fig. 10a) support these conclusions. XRD peaks that originate from the θ-phase, Mg_2Ge, W-phase and Al_6Mn can be observed. XRD peaks that originate from the $S(Al_2CuMg)$, $\beta'(MgAg)$ and U(AlMgAg) phases are distinguished only after ECAP to all strains examined. Notably, the U-phase is a Laves phase with a hexagonal lattice structure ($P6_3/mmc$). Therefore, intense plastic straining leads to additional [23] precipitation of magnesium and silver containing $\beta'(MgAg)$ and U(AlMgAg) phases. Inspection of the calculated Ag–Al–Cu phase diagram shows that these phases are possible to achieve at 300 °C [27].

3.3. *Microstructural evolution associated with ECAP of the over-aged alloy*

Microstructure evolution in the OA is quite different. Figs. 11 and 12 depict OIM maps and TEM images of representative microstructures of the OA material subjected to ECAP to strains ranging from ∼1 to ∼12. After $\varepsilon \sim 1$, the evolution of well-defined three-dimensional arrays of LABs is observed within interiors of the initial grains (Fig. 11a). It is worth noting that the formation of GNBs with moderate-to-high misorientation aligned along the shear direction also takes place. However, these deformation bands are subdivided by LABs on subgrains or (sub)grains

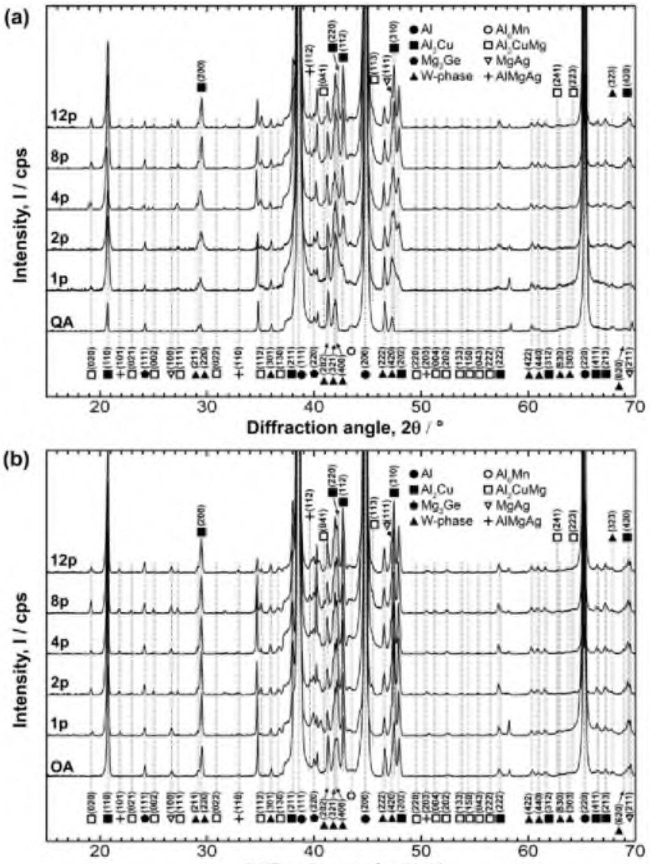

Fig. 10. X-Ray diffraction patterns taken from a QA sample that underwent ECAP (a) and OA (b).

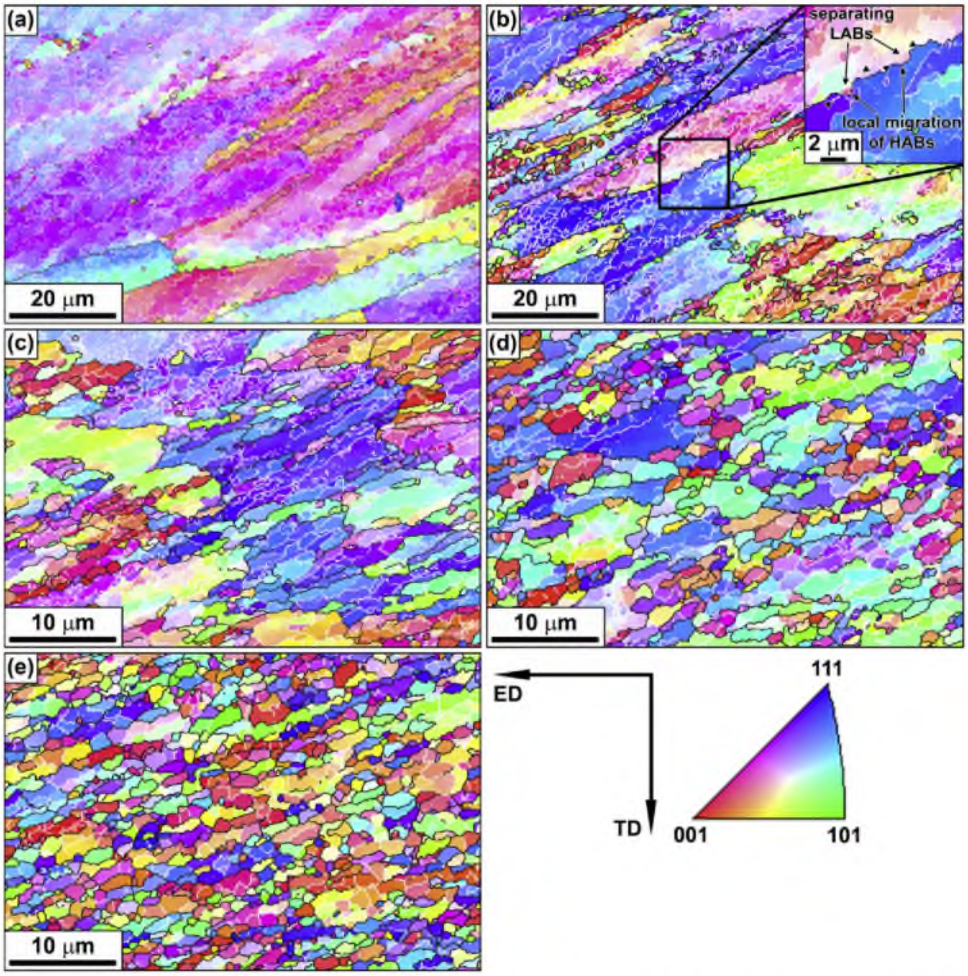

Fig. 11. Microstructural evolution of the OA subjected to ECAP with strains of $\varepsilon \sim 1$ (a), $\varepsilon \sim 2$ (b), $\varepsilon \sim 4$ (c), $\varepsilon \sim 8$ (d) and $\varepsilon \sim 12$ (e).

having an equiaxed shape (Fig. 12a). Therefore, over-aging highly promotes the formation of IDBs. In addition, initial boundaries become highly serrated (Fig. 11a). It can be clearly seen that the new (sub)grains or grains develop on the original boundaries or triple junctions through a mechanism of discontinuous DRX (DDRX). The local migration, or bulging, of initial boundaries leads to the formation of a nucleus, which is separated from the "parent" grain by the formation of a transverse deformation-induced LABs, which becomes the border between the bulged region and the parent grain. Therefore, DDRX is operative. However, the contribution of this recrystallization mechanism to overall DRX is minor. CDRX is primary mechanism of grain refinement in the OA. The rate of CDRX is increased due to the formation of 3D arrays of LABs. Owing to the superposition of CDRX and DDRX mechanisms, a number of (sub)grains and grains appear along the initial grain boundaries after $\varepsilon \sim 1$. Notably, the low density of lattice dislocations is observed (Table 1). It is apparent that these are attributed to the collection of dislocations in deformation-induced boundaries. No remarkable changes in a dispersion of secondary phases were found.

After $\varepsilon \sim 2$, new crystallites make up a mantle surrounding the initial grains (Fig. 11b). In addition, the formation of new grains takes place within interiors of initial grains and original boundaries. Extensive strain-induced grain boundary migration providing their local bulging (Fig. 11b) promotes DDRX. Crystallites with an equiaxed shape evolved within interiors of initial grains (Fig. 12b) by the CDRX mechanism. A four-fold increase in the dislocation density after the second ECAP pass (Table 1) was identified. Most of the particles associated with secondary phases acquire an equiaxed shape and are situated on deformation-induced boundaries (Fig. 12b).

After four ECAP passes, a partially recrystallized structure evolves: recrystallized grains and (sub)grains form a recrystallized mantle, while core regions consist of equiaxed subgrains (Fig. 11c). Separate grains evolve even in the core regions (Fig. 11c). The dislocation density increases insignificantly (Table 1). The coarsening of second phase particles situated on deformation-induced HABs (Fig. 12c) is observed.

Processing to higher strains leads to an increased volume fraction of recrystallized grains (Table 1). At $\varepsilon \sim 8$, a number crystallites in core regions are (sub)grain or subgrains; these crystallites exhibit essentially an equiaxed shape and are alternate to one another. A two-fold decrease in lattice dislocation density takes place with increasing strain from ~4 to ~8. It is known [22] that mobile dislocations are trapped by LABs resulting in an increase in their misorientation. As a result, most of LABs located in the core regions transform into HABs. The formation of an almost fully recrystallized structure is observed after $\varepsilon \sim 12$ (Fig. 11d and e). Greater uniformity of the recrystallized structure is observed in the OA as opposed to the QA.

Fig. 13 shows a STEM image together with elemental mapping of Cu, Ag, Ge, Mn, Sc and Mg. Particles having an equiaxed shape and average size of ~50 nm are hypothesized to be the θ-phase. Two types of secondary phases are retained after ECAP. First, precipitation of the primary Mg_2Ge phase [23] remains unchanged. Second, the volume fraction and size of the ternary W-phase particles [23]

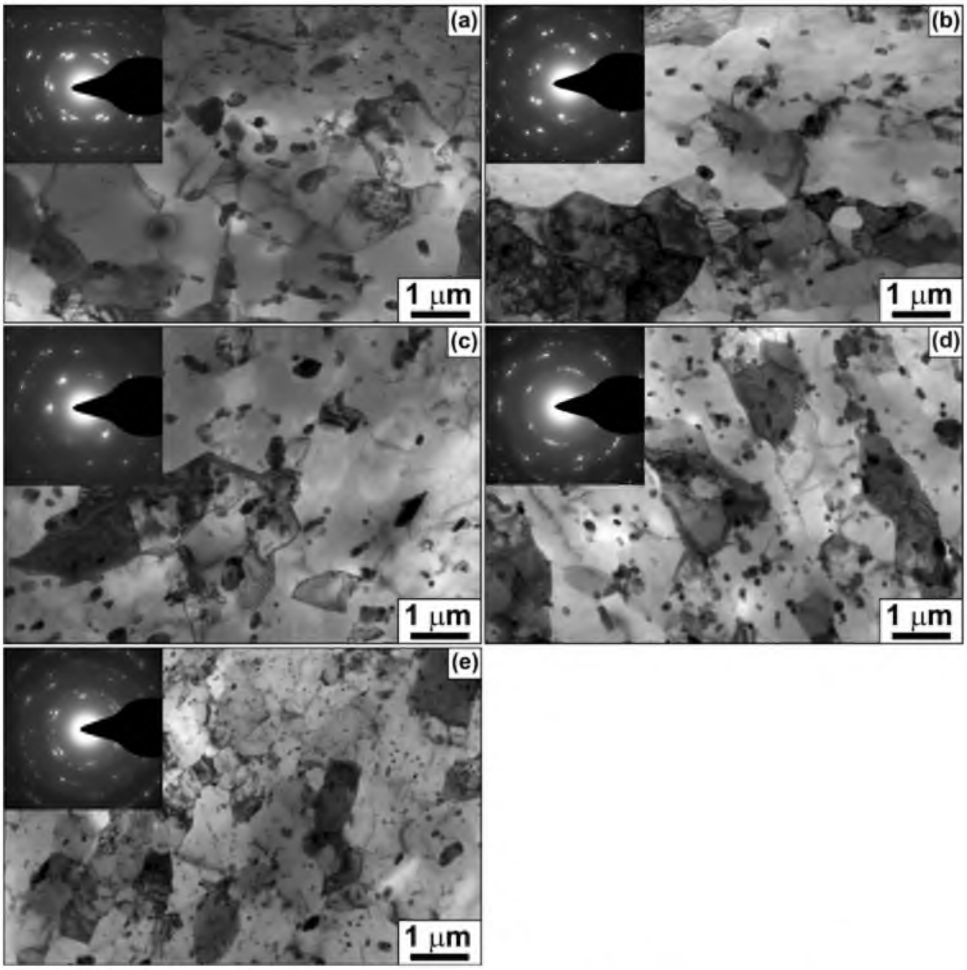

Fig. 12. Representative BF-TEM microstructures with diffraction patterns of the OA after ECAP to strains of $\varepsilon \sim 1$ (a), $\varepsilon \sim 2$ (b), $\varepsilon \sim 4$ (c), $\varepsilon \sim 8$ (c) and $\varepsilon \sim 12$ (e).

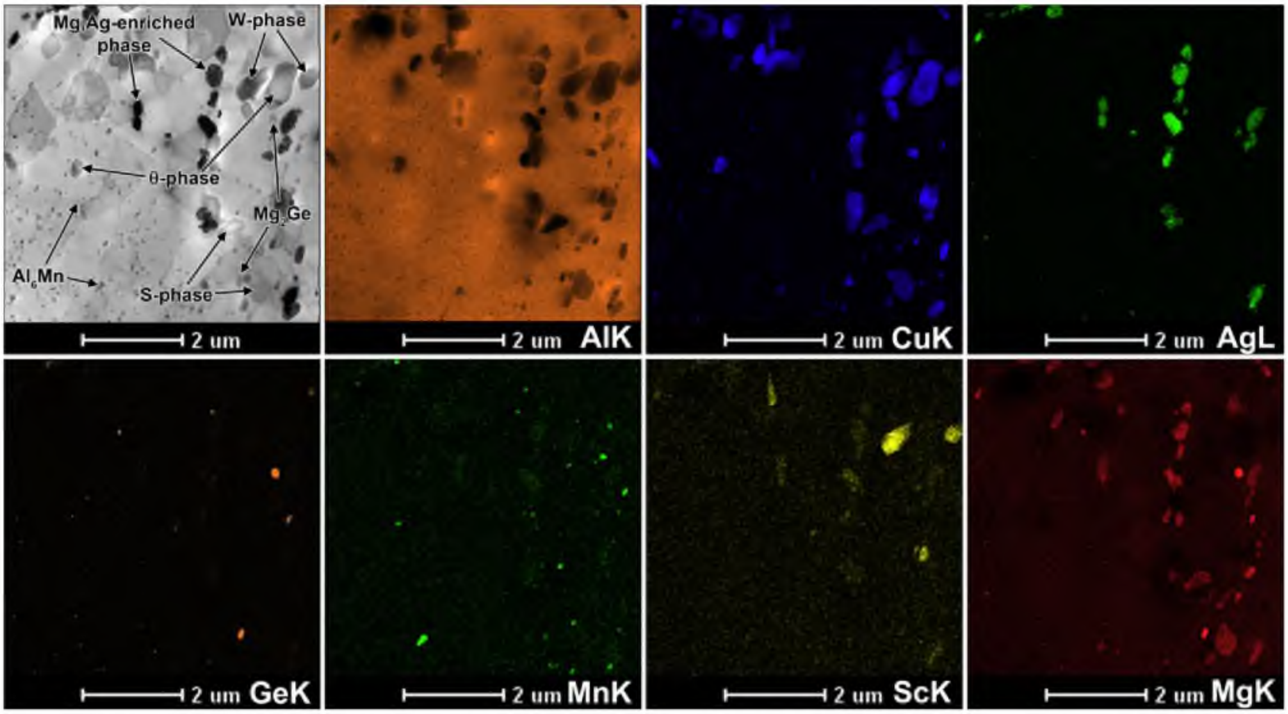

Fig. 13. STEM image and distribution of Al, Cu, Ag, Ge, Mn, Sc and Mg elements across a selected plane after 12 passes ECAP with the OA sample.

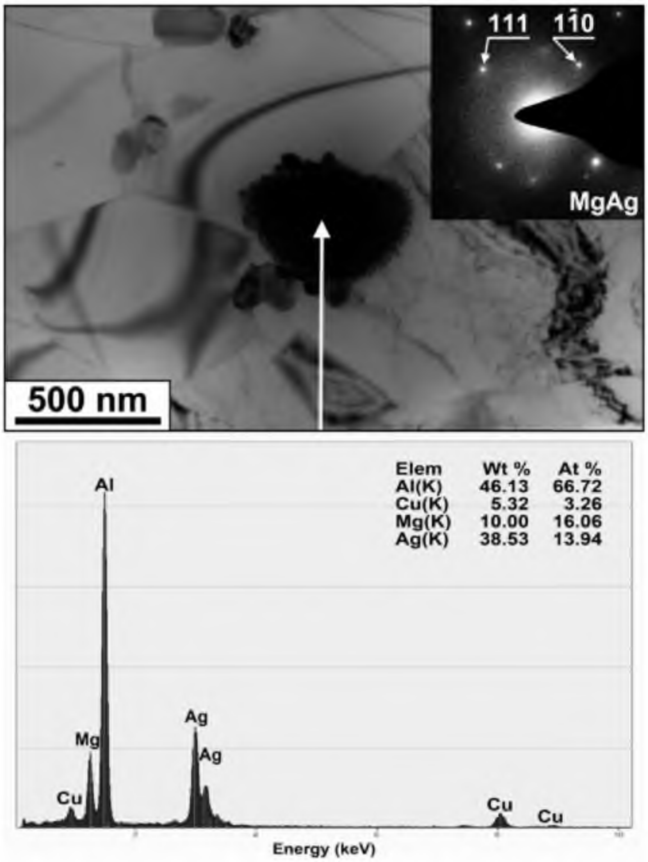

Fig. 14. TEM image and chemical composition of a MgAg particle in OA after ECAP to a strain of ~12.

are essentially retained. Notably, most of the hybrid particles are transformed to W-phase particles as a result of the dissolution of Sc-depleted θ-phase regions [23]. Thus, the most important change in a dispersion of secondary phase under ECAP is the dissolution of coarse Sc-enriched θ-phases and the precipitation of nanoscale θ-phase particles containing no Sc and Zr on boundaries with low- and high-angle misorientations. In contrast with the QA the nuclei of S-phases in the matrix were not found.

The X-ray diffraction data for the OA after ECAP are shown in Fig. 10b. XRD peaks that originate from the S-, β′- and U-phases were also distinguished. STEM analysis confirmed the formation of a Mg,Ag-enriched phase (Fig. 13). The SAED pattern shown in Fig. 14 originated from a compound with a cubic lattice identified as MgAg (*Pm*-3 *m*) (β′-phase). At $\varepsilon \sim 12$, the average size of those particles is ~0.5 μm. The precipitation of the U-phase was confirmed by X-ray diffraction alone.

3.4. Parameters of the deformed microstructure as a function of strain

The influence that strain has on the population of HABs and the average misorientation angle (θ_{av}) of deformation-induced boundaries are summarized in Fig. 15. It is seen (Figs. 15a and b) that the θ_{av}–ε and the HABs fraction *vs.* strain curves can be classified into one stage for the QA and into two stages for the OA. In the OA, the rapid increase in the θ_{av} value and fraction of HABs takes place at $\varepsilon \leq 4$; a gradual increase in these values with lower rates occurs upon further deformation (Figs. 15a and b). In the OA at $\varepsilon \geq 4$, and in the whole strain interval in the QA, the rates of misorientation growth can be approximated by linear function of cumulative strain, which is $\Delta\theta \propto 1.5^\circ \times \varepsilon$. Hence, in the OA, a rapid initial increase of θ_{av} provides an overall higher rate of grain formation in comparison with QA. Lacking of the first stage ceases the formation of fully recrystallized structure in the QA.

It is apparent that the first stage of microstructural evolution in the OA is attributed to the essentially uniform formation of 3D arrays of LABs (Figs. 11a&b and 12a&b). At second stage, the transformation of LABs to HABs controls the rate of new grain evolution. In the OA at $\varepsilon > 4$, this process provides the formation of deformation structure with a large fraction of 0.72 of HABs (Fig. 15b) and final average crystallite size of ~1.2 μm (Fig. 15d). It was shown by Humphreys et al. [28] that if the HABs fraction exceeds ~0.65, the structure can be considered as a grained one. Thus, over-aging provides the formation of grained structure. In the QA, no grained structure was attained even at $\varepsilon \sim 12$; the HABs fraction is ~0.59; average misorientation is ~25° (Figs. 15a and b).

At $\varepsilon \leq 2$, the grain aspect ratio (AR), defined as the ratio of the grain dimension in the shear direction to that in the transverse direction, in the QA is significantly higher than in the OA (Figs. 15c and d). In general, a reduction in spacing between both GNBs and IDBs takes place with strain, and the transverse IDB spacing approaches a steady state at $\varepsilon \leq 4$ in the QA and at $\varepsilon \leq 2$ in the OA (Fig. 15c and d) until their separation approaches the size of (sub)grains. The break-up of the deformation ribbon into (sub)grains with low AR occurs (Fig. 15c and d). As a result, in the OA, the recrystallized grains and (sub)grains exhibit essentially equiaxed shape at $\varepsilon \geq 2$, and in the QA at $\varepsilon \geq 4$ (Figs. 15c and d). It is worth noting that at $\varepsilon > 4$, the size of deformation-induced crystallites is almost the same in both states of the present alloy (Fig. 15c and d).

4. Discussion

4.1. Deformation structure

Grain refinement occurs during ECAP in the alloy both after quenching and over-aging. The rate of grain refinement is higher in the OA due to the fact that the rate of grain refinement is controlled by the formation of deformation-induced LABs at $\varepsilon \leq 2$. As shown above, two DRX mechanisms were found to be operative in the present alloy: DDRX and CDRX. CDRX yields the primary contribution in grain refinement in both states of the alloy. The difference in a rate of DRX process in the two states of the alloy results from the strong effect of over-aging on the uniformity of the dislocation glide. In addition, boundary precipitations resulting from over-aging play facilitate DDRX.

Regarding CDRX, the uniform formation of LABs in 3D arrays is a prerequisite condition for their transformation into HABs with a high rate upon further straining [22]. In the OA, the presence of first stage of grain refinement (Figs. 15a and b) is attributed to the fact that a dispersion of coarse and defect-free particles provides a homogeneous dislocation glide within the aluminum matrix. This homogeneity significantly reduces the average path length required for the rearrangement of lattice dislocations by climbing or cross-slipping to comprise an IDB facilitating the accumulation of lattice dislocations in these LABs.

In contrast, CDRX in the QA material occurs in a highly heterogeneous manner due to precipitation of small deformable plates of the Ω-phase. It is known [11,29] that if a certain number of dislocations shear a particle, the diameter of that particle will be reduced. The stress for further deformation then becomes smaller. The slip plane is softened, so that further slip will tend to move on the same plane, thus concentrating dislocation gliding into bands [12]. Therefore, well-defined deformation bands evolve in the QA due to localization of the dislocation glide. These deformation bands play a role of a precursor for the evolution of new grains.

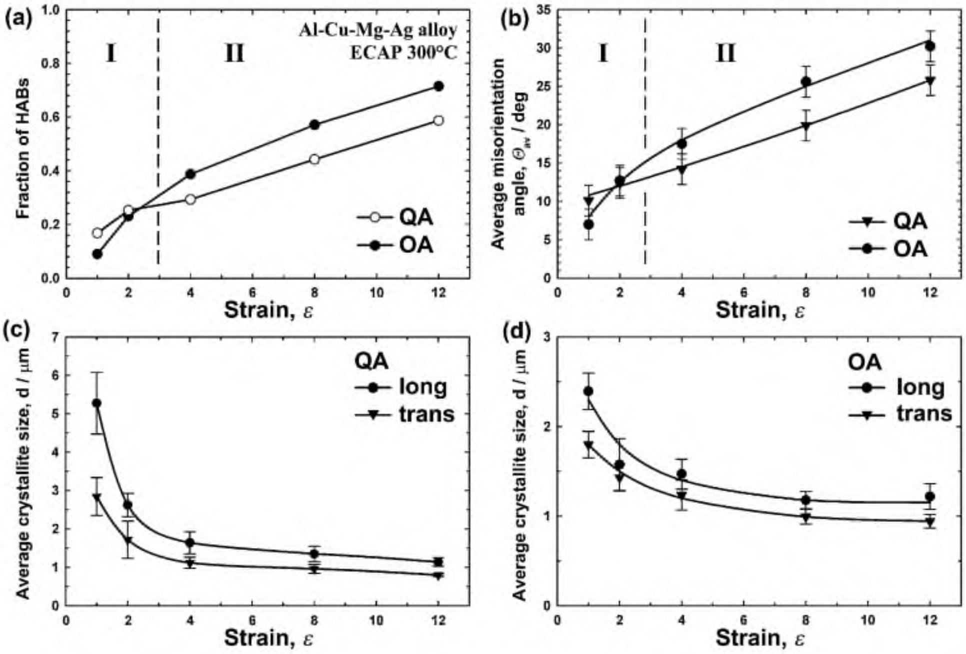

Fig. 15. Effect of strain on population of HAGBs (a) and average misorientation angle of deformation-induced boundaries, θ_{av} (b), the crystallite size *d* of QA (c), the crystallite size *d* of OA (d).

The same size of grains and (sub)grains in the QA and OA at $\varepsilon > 4$ is attributed to deformation-induced precipitations in the QA and changes in a dispersion of secondary phases in the OA. The nanoscale second-phase particles effectively pin boundary migration. As a result, 3D arrays of deformation-induced boundaries become highly stable and the recrystallization structure evolves through a CDRX mechanism primarily in both states of the Al–Cu–Mg–Ag-Sc alloy.

Regarding DDRX, the formation of LABs divides the bulged region from the "parent" grain; a DDRX nucleus evolves [30]. The formation of disperse secondary phases that occurs with over-aging highly promotes DDRX. Initial boundary bulging is a prelude to DDRX [11,30]. This bulged configuration is unstable [11,31]. Numerous secondary phase boundary particles arise from over-aging, and anchor initial boundaries triggering DDRX. Moreover, over-aging that facilitates the formation of LABs promotes the separation of the bulged region from the "parent" grain. By comparison, in the QA material, a bridging dislocation wall forms and anchors the bulged grain boundary [11]. However, their density is low.

No extensive growth of isolated nuclei into a surrounding deformed matrix occurs due to the fact that deformation structures contain relatively low energy levels stored in the form of free dislocations. Driving pressure due to stored dislocation [11] was calculated by method [31] and is $\sim 4.8 \times 10^4\,\mathrm{N\,m^{-2}}$ and $\sim 3.2 \times 10^4\,\mathrm{N\,m^{-2}}$ for the QA and the OA after $\varepsilon \sim 2$, respectively. Therefore, the anchoring of the bulged grain boundary and easy formation of "cutting" LABs are more important for DDRX than high driving pressure.

4.2. Precipitation behavior during ECAP.

It is known [6,29,32] that extensive ECAP suppresses the formation of metastable transition phases. Only thermodynamically stable phases are heterogeneously nucleated at the grain boundaries [6,29,32] during and after ECAP in the Al–Cu alloys. No indication of specific precursor formation was found in the present study. However, a unique precipitation sequence was found in different states of the Al–Cu–Mg–Ag alloy during ECAP.

4.2.1. Deformation-induced precipitation in the quenched alloy.

The following precipitation sequence takes place in the QA during ECAP:

SSSS→Ω-phase→θ-/S-phases

First, the passage of ECAP induces the decomposition of a supersaturated solid solution that leads to the homogeneous precipitation of coherent plates of the metastable Ω-phase. The segregation of Ag and Mg to the $(0\,0\,1)\Omega//(1\,1\,1)_\alpha$ interface accommodates a large misfit that exists normal to the broad face of Ω plates and decelerates the rate of coarsening at $T \leq 200\,^\circ\mathrm{C}$ [14,15]. It is known [12] that dislocation shearing forms the mismatched interfaces in the Ω-phase. A step with a high strain field around it created by shearing (Fig. 16) [12]. In addition, this step becomes a high energy boundary, and, therefore, such the interface is not favorable to form [12]. However, in contrast with room temperature [12], the Ag and Mg redistribution may occur from the broad face of the plate to the terrace of the migrating thickening ledge and the Cu flux through the matrix (Fig. 16) highly decrease the misfit [14,15] making this step coherent. Such the ledge created by the cutting has low energy and, therefore, can be easily formed. This

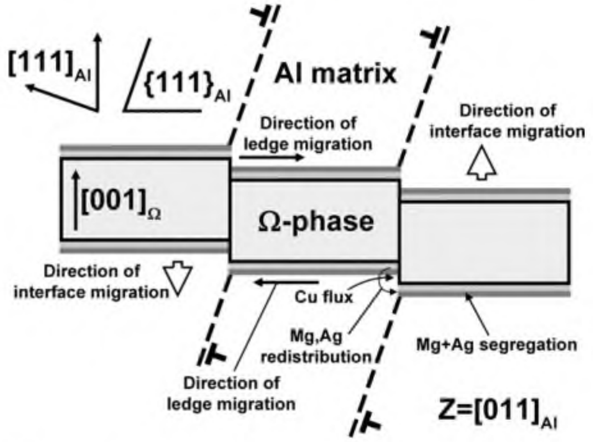

Fig. 16. Schematic showing of coarsening process of Ω-phase plate by deformation.

is why the single cutting (Fig. 16) is thermodynamically favorable at 300 °C, and slip localization is easy to occur in the QA due to deformation-induced precipitation of the Ω-phase at $\varepsilon \leq 2$.

At 300 °C, the amount of dislocation shearing increases which creates a large displacement leading to coagulation and coarsening of the Ω-phase. The coagulation could involve the ledge migration (Fig. 16) [14]. The shear offsets of the Ω plates provide the formation of two ledges by both sides of the plate (Fig. 16). The height and density of ledges on the plate surface of the Ω-phase tend to increase with strain. The inter-pass soaking leads to migration of ledges along the plate surface due to the high copper flux through the matrix to the terrace of the migrating thickening ledge (Fig. 16). This mechanism leads to increasing thickness of the Ω-phase plates. However, the mismatch is 9.3% that is high and Ω-phase/Al interfaces lose their coherency with increasing thickness [14,15]. The incoherent Ω-phase is metastable and has to dissolve in accordance with Gibbs–Thomson schema [26].

The following nucleation of the θ-phase occurs independently on grain boundaries [16,32], heterogeneously, or/and by transformation from the Ω-phase to the θ-phase. This transformation occurs by the rotation of Ω-phase particles concurrently with the depletion of Ag and Mg from the Ω-phase into growing particles of the S-phase and Al matrix. Heterogeneous nucleation of the S-phase takes place at the Ω-phase/Al interface. The formation of S-phase as a minor phase was reported in the literature [16,25] after artificial aging in Al–Cu–Mg–Ag alloys occurred with a Cu:Mg ratio closer to 10. It is apparent that plastic deformation promotes the formation of the S-phase in aluminum alloys with a high Cu:Mg ratio. In addition, precipitation of Ag containing stable phases (as β'- and U-phases) consumes Ag, which depleted from the Ω-phase. Notably, under static annealing, the formation of these Ag and Mg-enriched phases is suppressed by precipitation of the metastable Ω-phase. Thus, intense plastic straining provides the formation of highly dense dispersoids exerting increased Zener drag force [11] in the QA.

4.2.2. Precipitation process in the over-aged alloy

The primary precipitation event during ECAP is the dissolution of coarse particles with a Sc enriched θ-phase and the precipitation of nanoscale dispersoids of a Sc-depleted θ-phase. It is apparent that the Sc-enriched θ-phase (0.6–1.5%) is believed to be a metastable phase in comparison with the Sc depleted θ-phase [23]. The formation of deformation-induced boundaries encourages the nucleation of the θ-phase of equilibrium. Heterogeneous precipitation of the θ-phase dispersoids with significantly lower size eliminates coarse intragranular particles associated with the Sc enriched θ-phase precipitated during over-aging. Therefore, intense plastic straining could affect the type and size of stable phases significantly. A dispersion of the θ-phase exerts a high Zener force on deformation-induced LABs or HABs that suppresses their migration.

An inspection of the experimental data shows that intense plastic straining promotes the formation of Ag and Mg-containing β'- and U-phases after one pass of ECAP. These precipitations are equilibrium phases [27]. However, their precipitations are hindered under static annealing condition. Thus, ECAP provides the formation of Ag and Mg-containing phases that usually do not precipitate under annealing.

5. Conclusions

It was shown that the initial heat treatment highly affects microstructure evolution during ECAP to straining of ~12 at 300 °C in the Al–Cu–Mg–Ag alloy with small additions of zirconium and scandium. The key results are summarized as follows:

(a) Grain refinement occurs during ECAP in the alloy both after quenching (QA) and over-aging (OA). The rate of grain refinement is higher in the OA. Continuous DRX yields the primary contribution in grain refinement in both states of the alloy. Discontinuous DRX is operative only in the OA. Its contribution to overall grain refinement process is minor.

(b) In the OA, the grain refinement process can be subdivided into two stages where (1) a steep increase in the fraction of high-angle boundaries and the average misorientation occurs initially and (2) a gradual increase in these structural parameters occurs at $\varepsilon > 4$. In the QA, there is only one stage where a gradual increase in the fraction of high-angle boundaries and the average misorientation occurs at all strains. At $\varepsilon \leq 4$, acceleration of DRX occurs due to uniform formation of 3D arrays of low-angle boundaries followed by their eventual conversion into high-angle boundaries in the OA. In the QA, the formation of microbands persisted, thereby leading to the formation of new grains, and CDRX occurs in a localized manner.

(c) ECAP strongly influences precipitation reactions. In the QA, the precipitation of coherent particles adopting the Ω-phase having plate-like shape takes place at $\varepsilon \leq 1$. Further strain leads to a shearing offset of these particles owing to localized dislocation glide. Next, the dissolution of Ω-phase particles occurs along with the precipitation of θ-phase (Al_2Cu) and S-phase (Al_2CuMg) phases with an equiaxed shape.

(d) In the OA, the dissolution of relatively coarse particles of Sc enriched θ-phase followed by precipitation of nanoscale dispersoids of Sc depleted θ-phase on deformation-induced boundaries takes place. In addition, silver- and magnesium-rich particles of equilibrium β'(MgAg) and U(AlMgAg) phases precipitate during ECAP in the both states of the Al–Cu–Mg–Ag alloy.

Acknowledgments

This study was supported by the Federal Agency for Education of Russia, under Grant No. P875. The authors are grateful to the staff of the Joint Research Center at Belgorod State University for assistance with the mechanical and structural characterizations.

References

[1] R.Z. Valiev, T.G. Langdon, Prog. Mater. Sci. 51 (2006) 881–981.
[2] F. Musin, R. Kaibyshev, Y. Motohashi, G. Itoh, Metall. Mater. Trans. 35A (2004) 2383–2392.
[3] F. Musin, R. Kaibyshev, Y. Motohashi, T. Sakuma, G. Itoh, Mater. Trans. 43 (2002) 2370–2377.
[4] A. Mogucheva, R. Kaibyshev, Adv. Mater. Res. 89–91 (2010) 389–394.
[5] R. Kaibyshev, D. Tagirov, A. Mogucheva, Adv. Eng. Mater. 12 (2010) 735–739.
[6] I. Mazurina, T. Sakai, H. Miura, O. Sitdikov, R. Kaibyshev, Mater. Sci. Eng. A 473 (2008) 297–305.
[7] I. Mazurina, T. Sakai, H. Miura, O. Sitdikov, R. Kaibyshev, Mater. Sci. Eng. A 486 (2008) 662–671.
[8] I. Mazurina, T. Sakai, H. Miura, O. Sitdikov, R. Kaibyshev, Mater. Trans. 50 (2009) 101–110.
[9] Y. Huang, J.D. Robson, P.B. Prangnell, Acta Mater. 58 (2010) 1643–1657.
[10] P.J. Apps, J.R. Bowen, P.B. Prangnell, Acta Mater. 51 (2003) 2811–2822.
[11] F.J. Humphreys, M. Hatherly, Recrystallization, Related Annealing Phenomena, second ed., Elsevier, Oxford, 2004.
[12] B.Q. Li, F.E. Wawner, Acta Metall. 46 (1998) 5483–5490.
[13] J.F. Nie, B.C. Muddle, Scripta Mater. 42 (2000) 409–413.
[14] C.R. Hutchinson, X. Fan, S.J. Pennycook, G.J. Shiflet, Acta Mater. 49 (2001) 2827–2841.
[15] R.W. Fonda, W.A. Cassada, G.J. Shiflet, Acta Metal. Mater. 40 (1992) 2539–2546.
[16] L. Bakavos, P.B. Prangnell, B. Besb, F. Eberl, Mater. Sci. Eng. A 491 (2008) 214–223.
[17] S.P. Ringer, K. Hono, I.J. Polmear, T. Sakurai, Acta Mater. 44 (1996) 1883–1898.
[18] S.P. Ringer, W. Yeung, B.C. Muddle, I.J. Polmear, Acta Metal. Mater. 42 (1994) 1715–1725.
[19] Y. Iwahashi, Z. Horita, M. Nemoto, T.G. Langdon, Acta Mater. 45 (1997) 4733–4741.
[20] P.B. Hirsch, A. Howie, R.B. Nicholson, D.W. Pashley, M.J. Whelan, Electron microscopy of thin crystals, second ed., Krieger, New York, 1977.

[21] J.C. Russ, R.T. Dehoff, Practical Stereology, second ed., Kluwer Academic/Plenum, New York, 2000.
[22] R. Kaibyshev, K. Shipilova, F. Musin, Y. Motohashi, Mater. Sci. Eng. A 396 (2005) 341–351.
[23] M. Gazizov, V. Teleshov, V. Zakharov, R. Kaibyshev, J.Alloys Compd. 509 (2011) 9497–9507.
[24] D.A. Hughes, N. Hansen, D.J. Bammann, Scripta Mater. 48 (2003) 147–153.
[25] S.C. Wang, M.J. Starink, Int. Mater. Rev. 50 (2005) 193–215.
[26] D.A. Porter, K.E. Esterling, M. Sherif, Phase Transformation in Metals and Alloys, third ed., CRS Press, 2009.
[27] V. Raghavan, J. Phase Equilib. Diffus. 31 (2010) 297–299.
[28] F.J. Humphreys, P.B. Prangnell, J.R. Bowen, A. Gholinia, C. Harris, Phil. Trans. R. Soc. Lond. 357A (1999) 1663–1681.
[29] I. Nikulin, A. Kipelova, S. Malopheyev, R. Kaibyshev, Acta Mater. 60 (2012) 487–497.
[30] M. Murayana, Z. Horita, K. Hono, Acta Mater. 49 (2001) 21–29.
[31] O. Sitdikov, R. Kaibyshev, Mater. Trans. 42 (2001) 1928–1937.
[32] Y. Huang, J.D. Robson, P.B. Prangnell, Acta Mater. 58 (2010) 1643–1657.